THE ASTROPHYSICAL JOURNAL, 458:136–148, 1996 February 10

THE SUBARCSECOND RADIO STRUCTURE IN NGC 1068. I. OBSERVATIONS AND RESULTS

J. F. GALLIMORE,[1] S. A. BAUM, AND C. P. O'DEA
Space Telescope Science Institute, 3700 San Martin Drive, Baltimore, MD 21218

AND

A. PEDLAR
NRAL, Jodrell Bank, Macclesfield, Cheshire, England SK11 9DL, UK
Received 1995 May 26; accepted 1995 August 15

ABSTRACT

We present the results of new and archival multifrequency MERLIN and VLA observations of the hybrid starburst/Seyfert galaxy NGC 1068, with emphasis on the subarcsecond radio "triple" and its associated synchrotron-emitting jet. These results include measurements of the radio continuum spectrum and trajectory of the radio jet, the sizes and minimum energy properties of the compact features, and linear polarization at 22 GHz.

Between $\nu = 1.4$ and 22 GHz the northeastern and central components (NE and C) have steep spectra: $\alpha = -1.04 \pm 0.05$ and -0.67 ± 0.04, respectively ($S_\nu \propto \nu^\alpha$). The spectrum of the subarcsecond jet flattens locally at components NE and C, implying either compression or reacceleration. The southern component (S) has a very flat spectrum, $\alpha = -0.08 \pm 0.05$ between 1.4 and 22 GHz. The brightness temperatures of the compact features making up component S (subcomponents S1 and S2) are low, $T_b \sim 3 \times 10^5$ K at 5 GHz.

The radio jet bends abruptly at component C from an initial P.A. $\sim 12°$ to P.A. $\sim 30°$. Contrary to the findings of Ulvestad, Neff, & Wilson (1987), we find no evidence for a gradual, C-shaped bending of the radio jet. The minimum pressures of the compact features are comparable to those of the surrounding narrow-line region.

We report $\sim$4–5 σ detections of linear polarization in the directions of components NE and S. The polarization is detected at 22 GHz with 0.″25 resolution, but not in the more sensitive 15 GHz data with 0.″13 resolution. This result indicates that there may be substantial Faraday depolarization toward or within the subarcsecond radio structure.

Subject headings: galaxies: individual: (NGC 1068) — galaxies: jets — galaxies: Seyfert — galaxies: structure — radio continuum: galaxies

1. INTRODUCTION

The barred Sb galaxy NGC 1068 is one of the nearest and brightest Seyfert galaxies. As such, it has been exhaustively studied over all wavebands. Among Seyfert nuclei NGC 1068 stands out as a bright radio source (3C 71). Through aperture synthesis techniques the radio continuum emission is resolved into bright structures ranging in size from a few kiloparsecs, which is the scale of the star-forming inner spiral arms (Helfer & Blitz 1995; Neff et al. 1994; Planesas, Scoville, & Myers 1991; Telesco & Decher 1988; Myers & Scoville 1987; Wynn-Williams, Becklin, & Scoville 1985; see also Fig. 1), down to a few parsecs within the nucleus (Ulvestad, Neff, & Wilson 1987 [UNW]; Wilson & Ulvestad 1983; van der Hulst, Hummel, & Dickey 1982). Illustrated in Figures 1 and 2, the large-scale radio emission is dominated by a vaguely linear but highly structured source that is $\sim$13″ (1.3 kpc) in length. (We adopt a distance of 22 Mpc for NGC 1068, appropriate for $H_0 = 50$ km s^{-1} Mpc^{-1}; the scaling at this distance is 1″ $\approx$ 100 pc). The integrated radio continuum spectrum of this linear source is steep, with spectral index $\alpha \lesssim -1$ ($S_\nu \propto \nu^\alpha$; e.g., Wilson & Ulvestad 1987), consistent with optically thin, incoherent synchrotron emission. The "linear" source is thus usually interpreted as a collimated kiloparsec-scale radio jet (Wilson & Ulvestad 1982, 1983, 1987; Pedlar et al. 1983), analogous to the larger and more luminous radio jets observed in radio galaxies and radio-loud QSOs.

The brightest radio emission comes from the inner arcsecond of the nucleus and, with resolution better than 0.″3 (FWHM), resolves into a bent triple source. Our new images of the triple source are presented in Figures 1, 2, and 3, which serve to illustrate the following description. The principal, compact features are labeled as *component C*, the bright central component; *component NE*, the bright, extended feature located $\sim$0.″3 ($\sim$30 pc in projection) along p.a. = 31° from component C; and *component S*, the fainter component lying $\sim$0.″3 (30 pc) south of component C (along P.A. $\sim$ 190°). With resolution better than 0.″1, the southernmost component of the subarcsecond triple resolves into two subcomponents aligned roughly north–south (along P.A. = 4°). We refer to the northernmost (southernmost) subcomponent of component S as S1 (S2).

The nature of these compact radio features, or components, has been under debate. Van der Hulst et al. (1982) argued against a collimated jet origin because the components do not align but rather bend through an angle of $\sim$20°. Sensitive aperture synthesis images of the subarcsecond structure were obtained by UNW who detected the faint linear features connecting the components (see Figs. 2 and 3). They suggested that the compact features do indeed arise in the collimated jet but that the jet bends, perhaps as a result of ram pressure between the jet and the streaming interstellar medium surrounding the active nucleus.

[1] Also Astronomy Department, University of Maryland, College Park, MD 20742.

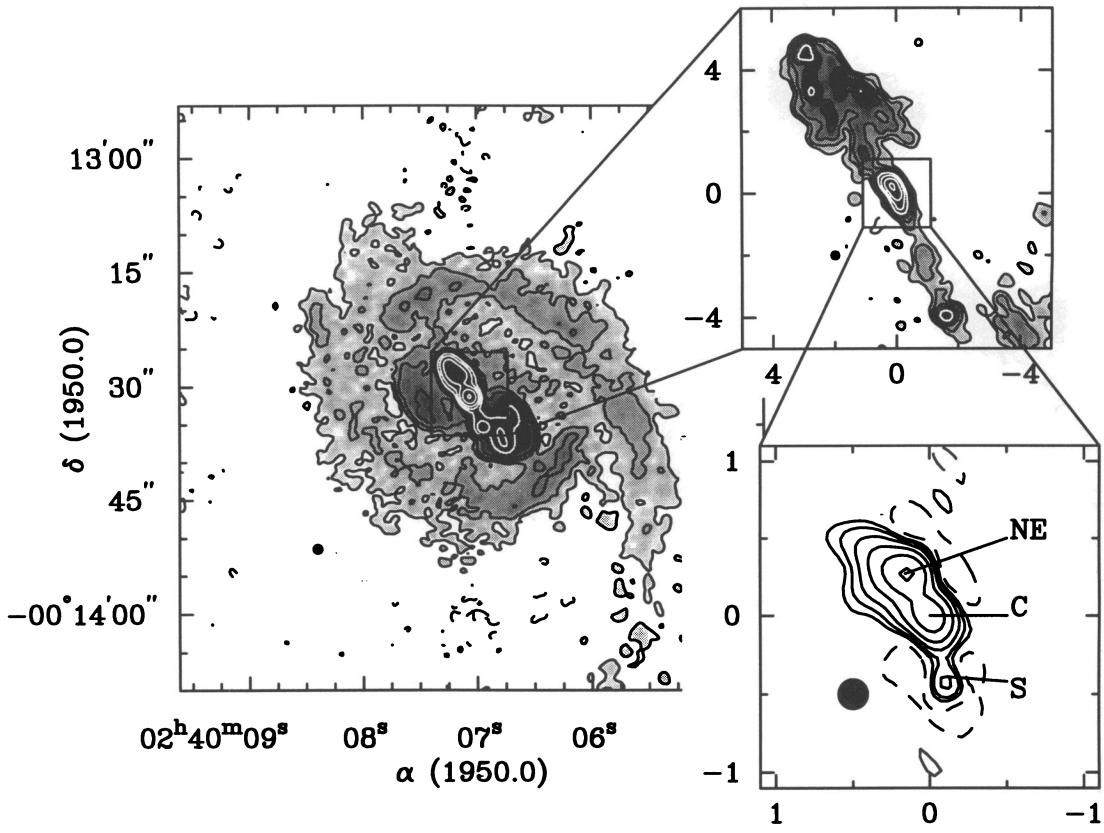

FIG. 1.—New aperture synthesis images of NGC 1068 at 18 cm wavelength. Contours are overlaid on grayscale with a logarithmic stretch. The lowest contour levels are ± 3 σ, and the higher contour levels scale exponentially to 90% of the peak flux in the image. The beam size (FWHM) is indicated by a darkened ellipse located to the lower left of the brighter continuum structure. *Left panel:* VLA, A-array image. The beam is circular with FWHM 1".35. Contour levels are: *black:* −0.30, 0.30, 0.74, 1.84, 4.55, 11.28; and *white:* 28.0, 69.3, 172, 426, and 1055 mJy beam^{-1}. *Top right panel:* Combined MERLIN and VLA, A-array image. The axes are offsets from component C, labeled in units of arcseconds. The beam size is 0".3, circular. Contour levels are: *black:* −1.9, 1.9, 4.0, 7.6, 18.4; and *white:* 39.5, 84.8, 181.8, and 390 mJy beam^{-1}. *Lower right panel:* Superresolved MERLIN image. The axes are offsets from component C, labeled in units of arcseconds, and the principal components are labeled. The restoring beam is 0".2, circular. Contour levels are −5.47, 5.47, 11.5, 24.3, 51.4, 108, and 229 mJy beam^{-1}.

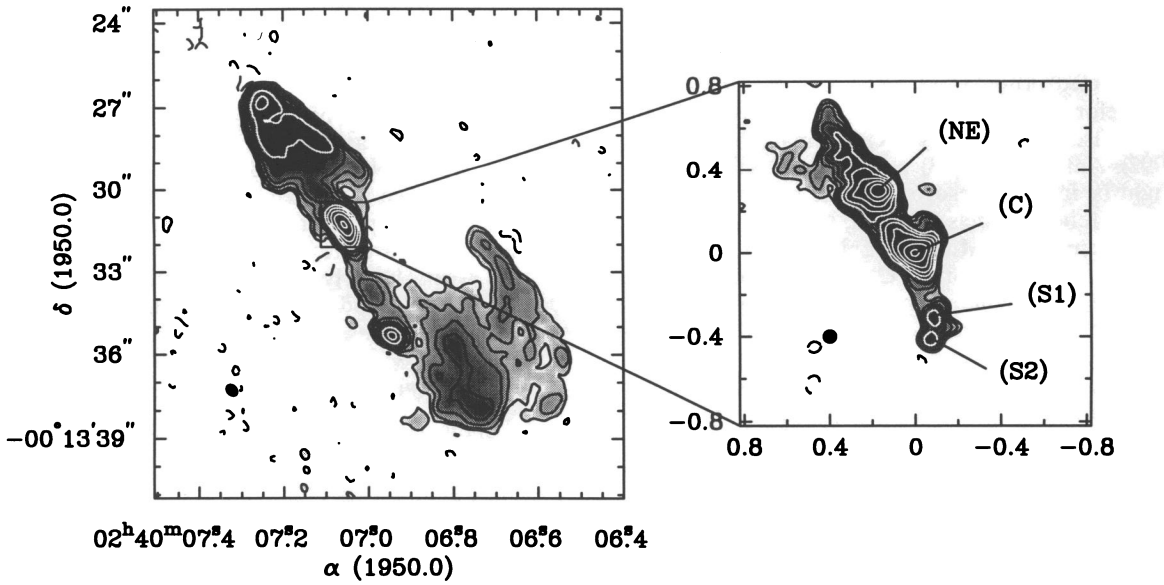

FIG. 2.—New aperture synthesis images of NGC 1068 at 6 cm wavelength. The presentation strategy is the same as in Fig. 1. *Left panel:* VLA, A-array image. The beam size is 0".49 × 0".38 along p.a. 47°. Contour levels: *black:* −0.40, 0.40, 0.82, 1.73, 3.61, 7.50; and *white:* 15.6, 32.4, 67.5, 140, and 292 mJy beam^{-1}. *Right panel:* MERLIN 6 cm image. The beam size is 65 mas, circular, and the principal components are labeled. Contour levels are: *black:* −0.86, 0.86, 1.38, 2.19, 3.50; and *white:* 5.59, 8.92, 14.2, 22.7, 36.2, 57.8 mJy beam^{-1}.

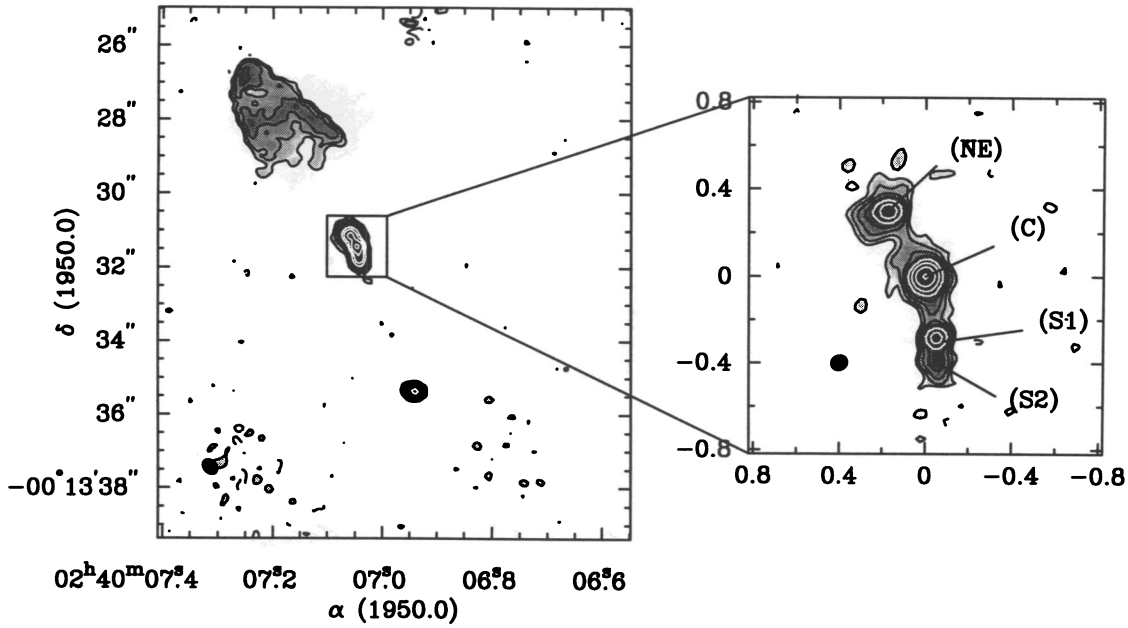

FIG. 3.—Archival 22 GHz (1.3 cm) images of NGC 1068. The presentation strategy is the same as in Fig. 1. *Left panel:* The (1993) VLA-B image. The beam size is 0".26 × 0".25 into p.a. −87°, and the rms noise is 0.27 mJy beam^{-1}. The contour levels are: *black:* −0.81, 0.81, 1.54, 2.92, 5.54; and *white:* 10.5, 19.9, 37.8, and 71.7 mJy beam^{-1}. *Right panel:* The (1992) VLA-A image. The beam size is 0".082 × 0".073 into p.a. −64°. The contour levels are, *black:* −0.801, 0.801, 1.38, 2.38, 4.09; and *white:* 7.05, 12.1, 20.9, and 36.0 mJy beam^{-1}.

There is further controversy over which, if any, of these components marks the location of the central power source, or "engine." UNW argue that component C best aligns with a compact feature in their 18 cm European VLBI network (EVN) image and, in analogy with the compact morphology of the nuclei of radio galaxies and QSOs, probably marks the location of the central engine. On the other hand, Claussen & Lo (1986) detected additional bright H_2O masers associated with component S (actually subcomponent S1; Gallimore et al. 1995b) that they suggest might occur in a dense, parsec-scale molecular disk, or "torus." Such a torus is posited to hide the broad-line region in this galaxy (e.g., Krolik & Begelman 1986, 1988; Antonucci & Miller 1985). However, we (Gallimore et al. 1995b) have detected bright H_2O maser emission near component C. Therefore, H_2O masers do not uniquely mark the central engine. Based on a 6 cm MERLIN image obtained by Muxlow (1992), Antonucci (1993) pointed out that the component S might be free-free absorbed by the putative torus as predicted by theoretical models (Neufeld, Maloney, & Conger 1994; Krolik & Lepp 1989). Muxlow et al. (1995) note that the 5–22 GHz spectrum of component C is not particularly flat. They suggest instead that one of the subcomponents of component S might be a synchrotron self-absorbed core and possibly the location of the central engine.

We have embarked on a detailed study of the radio nucleus of NGC 1068 to address the controversies over the nature of the subarcsecond radio structure, the origin of the H_2O maser emission, and the nature of the material that is obscuring the central engine at visible/UV wavelengths (e.g., Miller, Goodrich, & Matthews 1991; Antonucci & Miller 1985). To these ends we have obtained with the MERLIN telescope new subarcsecond resolution aperture synthesis images at 18 and 21 cm wavelength, and we have also collected both published (Kukula et al. 1995; Muxlow et al. 1995; UNW) and unpublished archival observations made with both the MERLIN and the Very Large Array[2] (VLA) synthesis telescopes. These observations collectively sample the centimeter-wave radio regime from 1.3 cm (22 GHz) to 21 cm (1.4 GHz) and resolve the three principal, subarcsecond radio components from one another. With these data we address the nature of the subarcsecond components based on their morphology and their radio continuum spectra.

In this paper (Paper I) we present an analysis of the new and archival radio continuum images and the continuum spectra extracted from these images. In a subsequent paper (Paper II; Gallimore, Baum, & O'Dea 1995a) we will discuss in more detail possible interpretations of these data taking into account *Hubble Space Telescope* observations (e.g., Macchetto et al. 1994) and observations at other wavebands.

This paper is organized as follows. In § 2, we summarize the new observations and the data reduction for both the new and archival images. The new radio continuum images are presented and described in § 3. The properties of the compact continuum features are presented and discussed in § 4. The properties of the radio jet are presented in § 5. In § 6 we report the detection of weak, linearly polarized continuum emission toward components NE and S. We conclude in § 7 with a summary of our principal results.

2. OBSERVATIONS AND DATA REDUCTION

All of the data were obtained either with the newly upgraded MERLIN or with the VLA in A-array. The MERLIN data were initially edited and calibrated using the OLAF-based pipeline at Jodrell Bank. The remaining data reduction for both the VLA and MERLIN observations was completed fol-

[2] The VLA is operated by the US National Radio Astronomy Observatory which is operated by Associated Universities, Inc., under cooperative agreement with the National Science Foundation.

TABLE 1

SUMMARY OF THE MERLIN AND VLA OBSERVING PARAMETERS

Synthesis Telescope (1)	ν (GHz) (2)	Date (3)	Time (hr) (4)	Flux Calibrator (5)	Flux (Jy) (6)	Phase Calibrator (7)	Flux (Jy) (8)	BW (MHz) (9)
M	1.416	93 Nov 19	6.07	3C 84	21.5	0237−027	0.25	7.9
M	1.658	93 Oct 19	2.39	3C 84	23.0	0237−027	0.29	15
A	1.415	92 Nov 19	1.88	3C 48	16.1	0320+053	2.8	6.2
A	1.674	94 May 9	3.32	3C 48	14.2	0320+053	2.4	13
A	4.802	94 May 9	2.79	3C 286	7.6	0238−084	2.2	25
A	22.46	92 Nov 19	6.36	3C 286	2.5	0235+164	7.5	100
B	22.46	93 Feb 26	6.18	3C 286	2.5	0237−027	1.2	100

NOTE.—Data are provided only for the previously unpublished observations. The columns are (1) aperture synthesis telescope (M = MERLIN, A = VLA, A-array, B = B-array), (2) frequency of observation in GHz, (3) date observed, (4) total time on source in hours, (5) flux calibrator, (6) calibrator flux in Jy, (7) phase calibrator, (8) phase calibrator flux in Jy, and (9) total bandwidth.

lowing standard procedures within the AIPS software package and using the computing facilities at Jodrell Bank, NRAO/Socorro, and STScI. We provide in this section an overview of the observing and data reduction techniques. Summaries of relevant observing and image parameters are provided in Tables 1 and 2. The previously unpublished new and archival synthesis images are displayed in Figures 1, 2, and 3. The 21 cm VLA and MERLIN images are not presented in this paper but are similar to those obtained at 18 cm wavelength.

2.1. *New MERLIN Observations*

As part of a program to observe neutral hydrogen absorption in NGC 1068 and test the recently upgraded array, we obtained new continuum images with the MERLIN telescope at 1.6 (18 cm) and 1.4 GHz (21 cm). Here we describe the data acquisition and reduction techniques employed for these new observations.

2.1.1. *The* 18 cm (1.6 GHz) *Observations*

NGC 1068 was observed using the entire eight-element MERLIN array, including the Lovell telescope, based at Jodrell Bank. These observations were taken in continuum mode with intermediate-frequency bands (IFs) offset slightly in frequency to optimize the coverage of the Fourier (u, v) plane. To ensure an accurate initial phase calibration, the phase calibrator was observed alternating frequently between scans of NGC 1068. The flux scale was set by the daily scan of 3C 286, according to the scale of Baars et al. (1977), and bootstrapped to scans of the intermediate flux/bandpass calibrator, 3C 84, and the phase calibrator, 0237−027. Initial phase calibration was determined from four cycles of self-calibration on the phase calibrator. To reduce confusion and aliasing from the more extended continuum flux originating away from the nuclear continuum and jet structures, we omitted the shortest baseline, namely the Mark II–Lovell baseline, from the continuum synthesis imaging.

Since NGC 1068 is situated near the celestial equator, the coverage in v (north–south baselines) determined by Earth-rotation synthesis is very poor. As a result, the initial synthesized map contained strong, modulated artifacts running north–south through the subarcsecond nuclear triple, and self-calibration was very slow to converge. To improve the coverage of the Fourier plane and thereby reduce the severity of the artifacts, we combined the MERLIN and VLA 18 cm "pseudo-continuum" data (§ 2.2.2). The VLA data were given only 10% of the weight of the MERLIN data to inhibit degradation of the angular resolution. We performed several iterations of phase-only self-calibration on the combined data. An image of the combined data set was made by Fourier-transforming the uniformly weighted visibilities into a "dirty" synthetic image. The dirty image was then deconvolved using the CLEAN algorithm (Clark 1980; Högbom 1974), tuned to remove only 5% of the brightest "point-" source per iteration and allowing frequent transfers between major and minor cycles. Such shallow CLEAN iterations were necessary to reduce spurious features introduced by the poor v-coverage. The MERLIN data were then calibrated against the CLEAN model synthesized from the combined arrays, and deconvolved in the same fashion. Described in Appendix A, we also synthesized images omitting baselines shorter than 200 kλ (corresponding to angular scales $\gtrsim 1''$). We then performed several iterations of self-calibration in phase which improved the resolution of the compact structure.

TABLE 2

SUMMARY OF THE PROPERTIES OF THE NEW MERLIN AND VLA IMAGES

Synthesis Telescope (1)	ν (GHz) (2)	rms (mJy) (3)	Beam Size Major (4)	Minor (5)	PA (6)
M	1.416	0.39	0.″35	0.″16	28°
M	1.658	0.33	0.″28	0.″15	−26°
A	1.415	0.18	2.″44	1.″48	−41°
A	1.674	0.099	1.″35	1.″35	0°
A	4.802	0.133	0.″49	0.″38	47°
A	22.46	0.34	0.″082	0.″073	66°
B	22.46	0.19	0.″26	0.″25	88°

NOTE.—Data are provided only for the previously unpublished observations. The columns are (1) aperture synthesis telescope (M = MERLIN, A = VLA, A-array, B = B-array), (2) frequency of observation in GHz, (3) rms image noise (mJy beam^{-1}), (4–6) Gaussian restoring beam properties (major axis, minor axis, and position angle). All image parameters are appropriate for uniformly weighted images, except for the A-array images at 1.4 and 1.6 GHz, which were weighted naturally.

2.1.2. *The* 21 cm (1.4 GHz) *Observations*

The techniques used for the 21 cm observations are identical to the 18 cm observations, except that we employed spectral line mode with the goal of detecting neutral hydrogen absorption. Bandpass calibration was performed on the spectral line data based on the scans of 3C 84. Again, the MERLIN data were self-calibrated against the weighted and combined VLA

and MERLIN sets (§ 2.2.1). Owing at least partially to a currently unsolved bandpass calibration problem, no H I absorption deeper than ~3 mJy was detected on the MERLIN baselines, so in the end we created a "pseudo-continuum" data set by averaging over all of the spectral line channels where the uncalibrated response was better than 50% that of the bandpass center. As for the 18 cm data, we also made images with the shorter baselines omitted (see Appendix A).

2.2. *New VLA Observations*

We have also obtained new VLA observations of NGC 1068 at 1.4, 1.7, and 5 GHz (21, 18, and 6 cm wavelengths). All of the observations were obtained in spectral line mode with the goal of detecting atomic and molecular absorption lines. In this paper we present only the data for the continuum channels. These data do not have the subarcsecond resolution necessary to study the small-scale radio jet. However, they do provide a measure of the flux missing in the MERLIN observations due to poor short-spacing coverage. In addition, the 1.4 and 1.7 GHz observations were used to assist the self-calibration of the new MERLIN observations (discussed above). The data acquisition and reduction techniques are discussed separately for each observed frequency.

2.2.1. *The* 21 cm *Observations*

We observed NGC 1068 at the redshifted 21 cm neutral hydrogen line with the A-array on 1992 November 22. The total, on-source integration time was 113 minutes, with individual scans interspersed among short scans of the phase calibrator, 0320 + 053, and longer scans of the flux/bandpass calibrator 3C 48. The observations were taken in the "4IF" spectral line mode with on-line Hanning smoothing to reduce the spectral "ringing" due to the Gibbs phenomenon. The total bandwidth covered by each intermediate frequency band (IF) is 3.125 MHz. To cover a larger effective velocity range, both dual-polarization (RR and LL pol.) IFs were tuned to recessional velocities slightly offset from each other but, in tandem, were centered at 1132 km s^{-1}, near the H I systemic velocity of NGC 1068 (1150 km s^{-1}; Brinks et al. 1992). After discarding the end four channels from each IF due to poor bandpass response, the total effective bandwidth obtained is 4.883 MHz over 50 channels, six of which overlap.

The amplitude and phase calibrations for the 21 cm observation were performed on the "channel 0" (or "pseudo-continuum") data, an average over the inner 75% of the observed bandpass for each IF. The flux scale and bandpass calibration were established by the scans of 3C 48. Amplitude and phase calibration solutions were generated from intermittent scans of 0320+053. We self-calibrated the pseudo-continuum data against successive CLEAN-deconvolved images of NGC 1068. We followed the conventional technique of calibrating only the phases initially, until the flux extracted in the CLEAN model was close to that apparent on short baselines. After that point, we performed two iterations of self-calibration including both amplitude and phase solutions with a coarse time resolution. A summary of the H I absorption results is provided in Gallimore et al. (1994).

2.2.2. *The* 18 cm (1.7 GHz) *Observations*

On 1994 March 13–14, again using the A-array, we observed NGC 1068 at the redshifted 1.7 GHz main line transitions of the OH radical. The on-source integration time was 100 minutes. We employed the "2AD" spectral line mode with on-line Hanning smoothing. To increase the total effective bandwidth, we tuned both circular polarizations to velocities offset from each other. The total effective bandwidth covered is 9.765 MHz (1770 km s^{-1}), resolved into 50 channels, each of width 195.3 kHz (35.4 km s^{-1}). The flux and phase calibrators were again 3C 48 and 0320+053, respectively. For the present work we use only the pseudo-continuum data; the spectral line data will be presented in a separate paper.

2.2.3. *The* 6 cm (5 GHz) *Observations*

We also observed the redshifted 6 cm line of H_2CO with the A-array on 1994 March 11. For this run we again used the "2AD" spectral line mode with on-line Hanning smoothing, but split the bandpass coverage into four overlapping cubes of total bandwidth 12.5 MHz. Only two of the four cubes could be observed simultaneously, so the observations were alternated between equal length scans for each cube pair for a total on-source integration of 2.8 hr. Neither line emission nor absorption was detected. Following the same general procedure as for the other A-array observations, we produced self-calibrated, CLEANed maps of the pseudo-continuum data. As for the 18 cm data, we present only the pseudo-continuum images, and the spectral line data will be discussed in a separate paper.

2.3. *Archival Observations*

We obtained archival subarcsecond resolution MERLIN and VLA observations of NGC 1068 to sample more completely the centimeter-wave spectrum. The MERLIN 6 cm image is also presented in Muxlow (1992) and Muxlow et al. (1995). All of the data reduction was performed by T. Muxlow and is discussed in Muxlow et al. (1995), so we provide only a terse overview here. The newer (1992/1993) VLA observations at 22 GHz are presented here for the first time. Here we describe the archival MERLIN and VLA data in turn.

2.3.1. *MERLIN* 6 cm *Image*

Muxlow and Antonucci observed NGC 1068 at 6 cm using the upgraded seven-element MERLIN telescope. The OLAF pipeline determined the initial calibration, and successive self-calibration was performed by an AIPS-based pipeline written by Tom Muxlow. The flux standard was again set by scans of 3C 286. Since, at 6 cm, the MERLIN telescope is insensitive to structures larger than about 1″–2″ in extent, the kiloparsec scale jet and starburst halo are resolved out by these observations, and the artifacts that plagued the observations at 18 and 21 cm are not present in the 6 cm map. The width of the Gaussian restoring beam used on the CLEAN-deconvolved image is 0.″065, and the rms noise is 0.29 mJy $beam^{-1}$. A more detailed account of the data reduction is provided in Muxlow et al. (1995).

2.3.2. *VLA Observations*

We obtained archival A-array data for NGC 1068 at 1.3 (22 GHz), 2 (14 GHz), and 3.6 cm (8 GHz) wavelengths. The 1983 observations at 1.3 cm and 2 cm, obtained by J. Ulvestad and A. Wilson, were originally published in UNW. Subsequent data at 1.3 cm were obtained by A. Wilson in 1992 and 1993. The 3.6 cm data were obtained by M. Kukula and A. Pedlar (Kukula et al. 1995).

The previously published 1.3 and 2 cm data were reduced from scratch following standard techniques. We performed several iterations of self-calibration on the complex phases which greatly reduced the random phase noise. Amplitude self-

calibration typically produced unrealistic solutions and degraded the synthesized images. Therefore, only the phase solutions were used for the final images. Both the 2 cm A-array and the 1.3 cm B-array observations were calibrated in polarization using 3C 286 as the linear polarization reference.

The 3.6 cm data were reduced by Kukula (Kukula et al. 1995). We tested the calibration by performing two iterations of phase-only self-calibration; only modest improvements to the synthesized image resulted from this self-calibration. As for the MERLIN 18 and 21 cm images, we also made images with the shorter baselines omitted (Appendix A).

3. RADIO CONTINUUM IMAGES

In Figures 1, 2, and 3 are displayed the previously unpublished 18 cm, 6 cm, and 1.3 cm radio continuum images. The 2 cm and 3.6 cm images can be found in UNW and Kukula et al. (1995), respectively. The three principal components (NE, C, and S) described in § 1 are resolved at each observed frequency. The doubling of component S into subcomponents S1 and S2 is fully resolved only on the 6 cm MERLIN and 1.3 cm VLA images. The 2 cm image only partially resolves S1 and S2. A qualitative comparison of the images reveals that both components C and NE greatly brighten between 1.3 and 18 cm, and it appears that component S also brightens, but to a lesser degree. Subcomponent S2 brightens relative to S1 between 1.3 cm and 6 cm (see Muxlow et al. 1995).

In addition to the compact components, there is emission extended on 0.″3–1″ scales that is detected on all of the images. Best resolved on the 6 cm MERLIN image (Fig. 2), the extended emission is vaguely linear and connects the principal components. There is additional structure at components NE and C extending away from (i.e., not necessarily aligned with) the linear features connecting the adjacent components. At component C there is an extension to the northwest giving a triangular (or conical?) shape to this component. At component NE the brighter emission continues to the northeast in the direction of the kiloparsec-scale radio lobe. As originally noted by UNW, there is also an extension to the east that is more clearly evident on the 1.3 and 2 cm VLA images. Much of this extended emission appears to brighten between 1.3 and 6 cm, indicating that it has a steep spectrum. By comparing the surface brightnesses between the 1.3 cm VLA and 6 cm MERLIN images, each having similar spatial resolution and sensitivities, we measure $-1.4 \lesssim \alpha \lesssim -0.65$ (see § 5.1) for the linear features connecting the adjacent components. The emission is therefore probably due to the incoherent synchrotron process in an optically thin plasma. The linear features are presumably associated with the small-scale jet that ultimately feeds the larger scale radio continuum structure in analogy with the pattern observed in more powerful radio galaxies.

As is apparent on the 2 cm and MERLIN 6 cm images, the extended emission concentrates near the compact components. In fitting two-dimensional Gaussians to components NE, C, and S, we found that the component sizes, deconvolved from the beam, typically doubled or trebled, from $\lesssim$ 0.″1–0.″15 to 0.″2–0.″3, between the high-resolution (1.3, 2, and 6 cm) and low-resolution (3.6, 18, and 21 cm) images. The cause of the "growth" of the components between the higher and lower resolution images is probably confusion with the extended emission within the 3.6, 18, and 21 cm beams. A significant portion of the "extended" flux at these wavebands probably arises from within ~0.″2 of the compact components.

Apart from the linear features, there is also emission extended on 1″–3″ scales to which the MERLIN 6 cm image is not sensitive but that is detected on the MERLIN 18 and 21 cm images. We estimate the size scale of this more diffuse emission by comparing the flux recovered by the VLA with the flux recovered by MERLIN. These fluxes, measured in a ~2″–3″ square region surrounding the subarcsecond triple, are provided in Table 3. The 21 cm MERLIN image recovers nearly all of the nuclear flux measured with the VLA, but about 7% is lost in the 18 cm image, presumably due to the shorter integration time and the correspondingly poorer (u, v) coverage than was achieved for the 21 cm image. In contrast, about 14% of the flux is missing in the MERLIN 6 cm image. At 6 cm MERLIN is insensitive to structures whose width is larger than ~1″–2″. Therefore, about 14% of the nuclear flux at 6 cm arises in extended emission distributed over ~1″–3″ scales. The combined MERLIN + VLA image (Fig. 1) shows that the arcsecond-scale emission near the nucleus aligns with large-scale jet structure.

4. THE COMPACT FEATURES

In this section we present the centimeter-wave continuum spectra of the compact radio components. The continuum fluxes were measured from the synthesized images, and the resulting spectra were modeled as single power laws. The results are presented in Tables 4 and 5 and plotted in Figure 4. We provide next (§ 4.1) a more detailed account of the measurement techniques and results. The sizes of subcomponents S1 and S2 were not well determined by two-dimensional analysis employed to measure the continuum fluxes. Described in § 4.2 we performed a one-dimensional analysis that better measures the subcomponent sizes. In § 4.3 we derive the minimum energy configuration properties of the compact components. The minimum energy properties are summarized in Table 6. We also estimate the minimum pressure in the synchrotron-emitting plasma, which we find to agree with pressures typical of the NLR gas.

4.1. *The Radio Spectra of the Compact Sources*

The principal difficulty in measuring the continuum flux densities for the compact components was confusion between adjacent components and with the underlying, extended continuum emission. For this reason we were unable to use aperture sums to measure the component fluxes but rather had to rely on a Gaussian fitting technique to reduce the contribution from confusing emission. On the MERLIN 6 cm and the VLA 2 and 1.3 cm images we were able reasonably to account for the extended emission by fitting simultaneously a constant offset and an elliptical Gaussian to the compact components. This

TABLE 3

INTEGRATED FLUXES OF THE RADIO NUCLEUS OF NGC 1068

λ (cm) (1)	S_ν(mJy) VLA-A (2)	S_ν(mJy) MERLIN (3)	Missing Flux (%) (4)	Box (arcsec) (5)
21.....	1497	1455	2.8	2.″8 × 3.″4
18.....	1445	1345	6.9	2.″8 × 3.″4
6.....	590	510	13.6	1.″5 × 1.″9

NOTE.—The columns are: (1) wavelength in cm, (2) integrated flux density measured by the VLA in A-array (mJy), (3) integrated flux density measured by the MERLIN telescope (mJy), (4) the percentage of A-array flux missing in the MERLIN image, and (5) the size of the box used to measure the fluxes.

TABLE 4

GAUSSIAN AND MOMENT ANALYSIS OF THE PRINCIPAL RADIO COMPONENTS

ν (GHz) (1)	Peak (mJy beam^{-1}) (2)	Flux (mJy) (3)	Major (mas) (4)	Minor (mas) (5)	P.A. (°) (6)
		Component NE			
1.417	271.8 (16.1)	498.6 (51.1)	$226.3^{249.6}_{201.8}$	$138.0^{162.0}_{110.7}$	56.3 (4.8)
1.658	256.1 (6.2)	381.6 (16.0)	$184.3^{193.9}_{174.5}$	$89.2^{101.5}_{75.3}$	68.5 (2.0)
4.993	40.2 (4.2)	170.8 (30.6)	$133.0^{149.8}_{115.7}$	$102.1^{116.6}_{86.8}$	57.9 (8.4)
8.465	79.9 (1.5)	95.9 (3.2)	$113.6^{122.3}_{104.4}$	$57.1^{70.3}_{40.3}$	39.4 (1.6)
14.940	20.6 (0.7)	38.2 (2.2)	$107.8^{114.8}_{100.5}$	$91.4^{98.5}_{83.9}$	−46.1 (2.6)
22.460	13.1 (0.8)	20.1 (2.0)	$64.2^{73.0}_{54.5}$	$48.8^{58.2}_{37.8}$	−78.9 (4.7)
22.460	15.8 (0.5)	21.7 (1.2)	$69.1^{74.2}_{63.7}$	$29.2^{36.6}_{19.5}$	−85.4 (2.5)
		Component C			
1.417	210.7 (20.3)	319.0 (53.2)	$188.7^{225.6}_{147.5}$	$91.7^{134.8}_{0.0}$	34.8 (7.8)
1.658	202.4 (8.5)	303.2 (22.0)	$201.6^{218.0}_{184.5}$	$67.2^{91.2}_{29.6}$	43.4 (3.4)
4.993	58.8 (3.9)	199.9 (22.9)	$113.7^{123.6}_{103.6}$	$88.7^{97.6}_{79.5}$	69.8 (5.4)
8.465	116.5 (3.6)	157.1 (8.5)	$167.7^{180.1}_{154.8}$	$49.4^{71.5}_{0.0}$	26.1 (2.5)
14.940	43.1 (1.5)	74.1 (4.5)	$103.4^{111.1}_{95.5}$	$80.0^{87.9}_{71.5}$	10.2 (2.9)
22.460	41.2 (0.8)	54.1 (1.8)	$48.8^{52.0}_{45.4}$	$38.5^{42.2}_{34.6}$	138.4 (1.6)
22.460	38.5 (0.7)	54.5 (1.7)	$54.0^{57.2}_{50.5}$	$54.0^{57.2}_{50.5}$	20.5 (1.5)
		Component S			
1.417	34.1 (3.0)	38.0 (5.7)	$153.3^{187.1}_{113.8}$	<98.8	14.8 (7.0)
1.658	34.4 (4.9)	35.1 (8.6)	$198.8^{252.4}_{136.2}$	<52.2	4.8 (11.5)
4.993 M.....	9.1 (0.6)	29.0 (3.3)	$187.0^{200.8}_{173.1}$	$74.7^{83.1}_{65.8}$	−3.0 (5.3)
8.465 M.....	32.5 (0.9)	38.6 (1.9)	$141.5^{153.5}_{128.9}$	<70.1	2.5 (2.3)
14.940 M.....	16.0 (0.4)	32.7 (1.3)	$169.4^{174.8}_{164.0}$	$45.4^{52.0}_{37.8}$	6.6 (1.8)
22.460 M.....	16.2 (0.5)	24.0 (1.2)	$131.6^{136.8}_{126.4}$	$106.5^{111.2}_{101.7}$	−3.3 (2.4)
22.460 M.....	17.1 (0.3)	31.0 (0.8)	$151.8^{154.9}_{148.7}$	$34.8^{38.3}_{30.9}$	2.5 (1.3)
		Component S1			
4.993	7.2 (0.4)	12.2 (1.1)	$72.0^{78.9}_{64.7}$	$33.2^{41.2}_{23.3}$	26.5 (4.4)
22.460	16.4 (0.6)	18.8 (1.1)	$42.9^{48.9}_{36.1}$	$5.6^{21.4}_{0.0}$	−13.4 (2.8)
22.460	16.5 (0.3)	19.1 (0.6)	$46.2^{49.9}_{42.3}$	$8.2^{18.4}_{0.0}$	11.6 (1.6)
		Component S2			
4.993	8.8 (0.4)	10.4 (0.8)	$33.2^{39.8}_{25.3}$	$23.2^{31.1}_{11.1}$	−63.7 (3.6)
22.460	5.3 (0.6)	7.8 (1.4)	$102.7^{119.4}_{85.0}$	<47.4	72.8 (8.6)
22.460	5.6 (0.3)	8.3 (0.3)	$76.7^{85.9}_{66.8}$	$34.8^{46.5}_{17.7}$	14.1 (4.6)

NOTES.—Fluxes, positions, and widths of the subarcsecond components measured by two-dimensional Gaussian fits or moment analysis (indicated by an "M" after the frequency). The errors, listed in parenthesis, are 1 σ. The columns are (1) frequency, (2) peak flux density, (3) total flux, (4) beam-deconvolved major axis length (FWHM), (5) minor axis length, and (6) position angle. The 1 σ range for the axis lengths are indicated by sub- and superscripts. The data for the first (second) 22.46 GHz listing under each component are measured from the 1983 (1992). Limits, where indicated, are 3 σ.

technique was not successful for the MERLIN 18 and 21 cm and the A-array 3.6 cm data because of the poorer resolution and confusion between adjacent components. To alleviate this problem, we filtered out the extended emission by omitting the shorter baselines during the Fourier-transform to the synthesized images (the equivalent of a high-pass filter for spatial frequencies). We also "superresolved" the images during the deconvolution process. The expense of these procedures is a greater uncertainty in the flux measurements than would be achieved in a simple aperture sum of an isolated compact feature. A more detailed account of the imaging procedure, the Gaussian-fitting technique, and the error analysis is provided in Appendix A.

The fluxes and sizes of the compact radio components measured by either Gaussian or moment analysis are included in Table 4, and the spectra are plotted in Figure 4. The continuum spectrum of each component is fairly linear (in log-log space) with two-point spectral indices between adjacent frequencies typically $\gtrsim -1.0$. To estimate the spectral indices we fit the spectrum of each principal component with a power-law model, $S_\nu = S_{1\,\mathrm{GHz}}(\nu/1\ \mathrm{GHz})^\alpha$. For this task we used the program GaussFit (Jeffreys et al. 1988), which uses an iterative robust parameter estimation technique that is relatively insensitive to outliers. Power-law models were also separately fitted to each of the high- and low-resolution flux density spectra, and we estimated the spectral indices of the subcomponents S1

TABLE 5

SPECTRAL INDEX FITS FOR THE SUBARCSECOND CONTINUUM COMPONENTS IN NGC 1068

Component (1)	S_ν (1 GHz) (2)	α (3)	χ^2_{red} (4)	d.o.f. (5)
Principal Components				
NE	670 (63)	−1.04 (0.05)	2.8	5
C	450 (52)	−0.67 (0.04)	1.3	5
S	40 (7)	−0.08 (0.05)	2.1	5
Southern Subcomponents				
S1	...	0.30 (0.06)	...	...
S2	...	−0.15 (0.08)	...	...

NOTE.—The model in $S_\nu = S_0(\nu/1\ \mathrm{GHz})^\alpha$. The columns are (1) component name, (2) S_0, total flux at 1 GHz (with 1 σ uncertainty), (3) the spectral index α (with uncertainty), (4) the reduced χ^2 statistic, and (5) the number of degrees of freedom in the model. The two-point spectral indices for the subcomponents S1 and S2 are provided in the last two rows.

TABLE 6

MINIMUM ENERGY CONFIGURATION PROPERTIES FOR THE COMPACT RADIO COMPONENTS

(1) Component	S2	S1	C	NE
(2) $S_{\nu 0}$ (mJy)	8.3	18.8	450	666
(3) ν_0 (GHz)	22.46	22.46	1.0	1.0
(4) α	−0.15	0.3	−0.67	−1.04
(5) d (parsecs)	2.8	4.9	5.4	4.5
(6) $L/10^5\ L_\odot$	3.36	1.16	8.81	9.16
(7) U_{min} (10^{55} ergs)	1.6	5.1	25	38
(8) $B(U_{min})$ (μgauss)	520	390	730	1200
(9) P_{min}/k (10^8K cm^{-3})	1.8	1.0	3.7	9.9

NOTE.—The rows are (1) the component name, (2) the flux density at (3) frequency ν_0, (4) the spectral index for the centimeter-wave spectrum, (5) the equivalent circular diameter of the component, (6) the radio luminosity integrated over the extrapolated power-law spectrum between 10 MHz and 100 GHz, (7) the minimum total energy, (8) the magnetic field strength at the minimum energy, and (9) the minimum pressure in the plasma. Rows (2)–(5) are based on the Gaussian analysis of the components, and rows (7)–(9) were calculated using the minimum energy assumption.

and S2 based on the ratios of their 1.3 cm and MERLIN 6 cm flux densities.

The results of the single power-law fits are listed in Table 5 and plotted (as a solid line) in Figure 4. The fits to the combined high- and low-resolution data are generally acceptable but poor, with reduced χ^2 values ranging from 1.3 to 2.8. This is not unexpected in view of the varying spatial resolution and sensitivity of these multifrequency observations, and also considering that the actual spectra may not be well-described by a single power law over the entire observed spectral range. The power-law fits nevertheless provide a reasonable description of the spectral behavior to compare the different components. The spectra of components NE and C are significantly steeper than the collective spectrum of component S. The spectral index of component NE is ~ -1, comparable to that of the synchrotron jet emission on tens of parsecs (§ 5.1) and kiloparsec-scales (see Wilson & Ulvestad 1987). The spectrum of component C is somewhat flatter, with $\alpha \sim -0.7$. In either case, the spectral indices derived from both the high- and low-resolution data compare well with those measured from the high-resolution data alone. This result suggests that, insofar as the spectra can be modeled by a single power law, any confusion with the underlying extended emission is probably small.

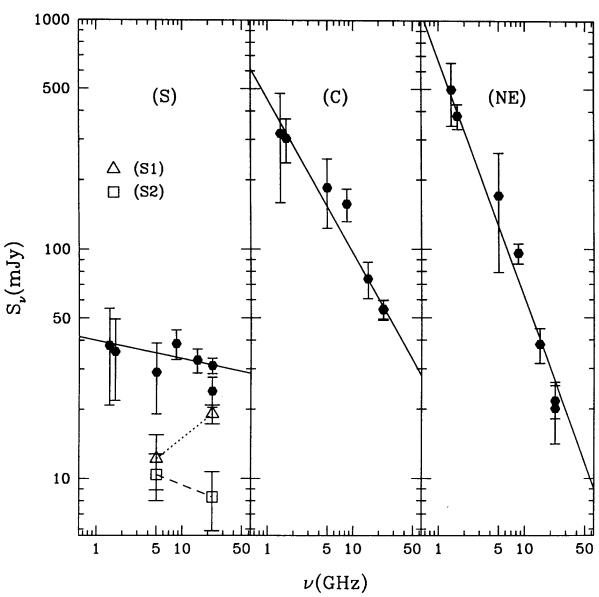

FIG. 4.—Radio continuum spectra of the subarcsecond triple in NGC 1068. The values in the panels from left to right are measured from components S, C, and NE, respectively. The filled hexagons are the measured fluxes with 3 σ error bars, and the solid lines represent the best-fit power-law spectrum (see Table 5). The fluxes of subcomponents S1 and S2 are included in the leftmost panel and are indicated by connected triangles and squares, respectively.

In contrast, the collective spectrum of component S is very flat, $\alpha \sim -0.1$ between 1.3 to 21 cm. This is somewhat surprising, since the flux densities measured for this component include contributions from both subcomponents S1 and S2 as well as the surrounding diffuse emission. Based on the total fluxes measured from the 1.3 cm and MERLIN 6 cm images, the spectrum of component S1 is inverted ($\alpha \sim 0.3$). Component S2 has a very flat spectrum between 1.3 and 6 cm, with $\alpha \sim -0.15$.

At 6 cm wavelength the subcomponents S1 and S2 contribute about 75% of the flux received from component S (Table 4); the remainder must arise in diffuse emission from within 0.″15 of the centroid of these subcomponents. At 1.3 cm, however, the diffuse emission is very faint and is undetected in the less sensitive 1983 data. Between 1.3 and 6 cm, then, the spectrum of the residual, diffuse emission surrounding subcomponents S1 and S2 is probably fairly flat. Our present data are unfortunately too noisy to determine well the spectrum of the diffuse emission; we estimate $\alpha = -0.38 \pm 0.44$ based on the residual (total − compact) fluxes on the 6 cm MERLIN and (1992) 1.3 cm A-array images. The contributions of the diffuse and compact (S1 and S2) radio emission extrapolated from 5 GHz down to 1.4 GHz account well for the total observed flux at 1.4 GHz. Based on the 5–22 GHz spectral indices, the extrapolated relative contributions at 1.4 GHz are 10, 8.3, and 12.6 mJy for the diffuse emission, and components S1 and S2, respectively. The total extrapolated flux is then 31 mJy, and the flux measured at 1.4 GHz is 38 ± 6 mJy (Table 4). Unless there is a precipitous cutoff in either of the spectra for components S1 and S2 between 1.4 and 5 GHz, the diffuse emission from component S must have a fairly flat spectrum. Measurement of the actual spectral behavior within component S will require higher resolution observations at a frequency lower than 5 GHz.

4.2. *Spatial Analysis*

In order to interpret the nature of the radio components and calculate, for example, their minimum energy configuration properties, it is necessary to have a good estimate of their sizes and brightness temperatures. For our purposes, the sizes determined by either Gaussian or moment analysis generally suffice (Table 4). The sizes measured for subcomponents S1 and S2 are however very uncertain. Part of the problem is that neither subcomponent is well fitted by a two-dimensional Gaussian, so errors in the width along any given axis are amplified by the poor quality of the fit along two axes simultaneously. To improve the accuracy of the measurements, we repeated the measurement for both subcomponents by extracting one-dimensional surface brightness profiles through the position of peak brightness. On the MERLIN 5 GHz image the minimum width (FWHM) of subcomponent S1 (S2) is 39.7 ± 5.1 mas (38.2 ± 4.7 mas), deconvolved from the beam. Using these widths, the 5 GHz brightness temperatures are $(2.6 \pm 0.3) \times 10^5$ and $(3.1 \pm 0.4) \times 10^5$ K for subcomponents S1 and S2, respectively.

T. W. B. Muxlow (personal communication) has cautioned that the image fidelity of the MERLIN 5 GHz image is insufficient for a reliable determination of the size of components S1 and S2. We therefore performed the same spatial analysis on the (1992) VLA 22 GHz image. The minimum width of subcomponent S1 is 43 ± 6 mas, consistent with the MERLIN measurement. The 22 GHz brightness temperature of S1 is $(1.1 \pm 0.2) \times 10^5$ K. Due to confusion with S1, the size of S2 cannot be determined on the 22 GHz images, so we will adopt the size measured from the MERLIN image.

4.3. *Minimum Energy Configuration Properties*

As an aid to understanding the nature of the synchrotron-emitting plasma, it is useful to have some estimate of the energy and magnetic field strength contained in the plasma; measurement of these properties requires, however, assumptions about the relative geometry and configuration of the plasma and associated magnetic fields. Burbidge (1956) derived a general formula estimating the minimum energy density (or pressure) contained in a synchrotron-emitting plasma based on its brightness, size, and continuum spectrum. Following the formulation of Moffet (1975), we present in Table 6 the minimum energy configuration properties of the subarcsecond components. Estimates of the spectral index, size, and brightness were based on the Gaussian analysis (Tables 4 and 5). We further assumed a spherical geometry for each component, with a diameter equal to the equivalent circular width based on the Gaussian fits to the FHWM of the component. For components NE and C we used the widths fitted to the (1992) 22 GHz image, and for subcomponents S1 and S2 we used those fitted to the MERLIN 5 GHz image. Electrons and protons were taken to carry equal amounts of energy.

The basic results are the following. The minimum energy magnetic field strengths are typically on the order of one milligauss. The minimum pressures are on the order of 10^8 km s^{-3}. Based on forbidden line ratios, the pressure in the NLR gas is $n_e T_e \sim 10^7$–10^8 km cm^{-3} (Shields & Oke 1975; Khachikian & Weedman 1971; Osterbrock & Parker 1965). That the pressures inferred for the NLR and synchrotron plasmas are comparable suggests the possibility that the jet is confined laterally by the surrounding NLR gas. It should be emphasized, however, that there is no evidence that the radio plasma in the subarcsecond jet in NGC 1068 is in its minimum energy configuration. In addition to this usual caveat, it should also be pointed out that the emission from subcomponents S1 and S2 may not be due to the synchrotron process but rather may be thermal in origin (see Paper II), in which case the minimum energy properties for these subcomponents are meaningless. We nevertheless include these inferred properties for completeness.

5. THE RADIO JET

In this section we discuss the continuum spectra and trajectory of the subarcsecond radio jet. The principal result is that the apparent bend in the radio jet at component C is probably both real and abrupt. The radio spectrum flattens at both components C and NE. Such spectral flattening indicates that at these components either more energetic particles are being introduced through reacceleration or that the synchrotron plasma is compressed (e.g., Scheuer & Williams 1968). We describe in turn the properties of the jet spectra (§ 5.1) and the trajectory (§ 5.2).

5.1. *The Radio Jet Spectra*

The radio spectral properties of the linear features connecting the compact components are important to the interpretation of the subarcsecond radio structure of NGC 1068. Unfortunately, the images presented here are diverse in their spatial sensitivities and resolutions, so it is difficult to determine the full centimeter-wave spectrum for the jet emission. The 1.3 and MERLIN 6 cm images share, however, similar spatial sensitivities, and we have measured the 1.3–1.6 cm spectral index of the jet as a function of distance along the jet from component S. Probably resulting as an artifact of the self-calibration method, there are subtle misalignments between the principal, compact components precluding a simple imaging of the spectral index distribution. We instead estimated the spectral index as a function of distance along the jet by taking the ratio of the peak cross-sectional flux densities at equally spaced positions between the principal components; the exact technique employed is discussed in more detail below in § 5.2.

The result is displayed in Figure 5. Starting at subcomponent S1, the spectrum is initially inverted, as was found using Gaussian analysis (§ 4.1). Broadly, the spectrum steepens with distance from component S1. The spectral indices reach an initial minimum of $\alpha = -0.65 \pm 0.02$ at $\sim 0\farcs2$ (20 parsecs) from component S1, and a secondary minimum of $\alpha = -1.4 \pm 0.09$ at $\sim 0\farcs15$ (15 parsecs) from component C ($0\farcs44$ along the jet from component S1). The spectra flatten locally at components C and NE, at which the respective spectral indices are -0.48 ± 0.01 and -0.86 ± 0.01 based on the cross-sectional analysis. Slightly steeper indices are found for components C and NE using Gaussian analysis (Table 5); this is probably the result of confusion between the jet and compact emission.

The broad trend of spectral steepening along the jet may be the result of ageing of the synchrotron electrons. The oldest material would have the steepest spectrum (e.g., Myers & Spangler 1985), so the trend found here places component S nearer the electron injection source (i.e., the central engine) than components C and NE, with NE being the relatively farthest downstream. However, the spectra of both components NE and C are flatter than those of the jet emission surrounding them, indicating that "younger" particles are

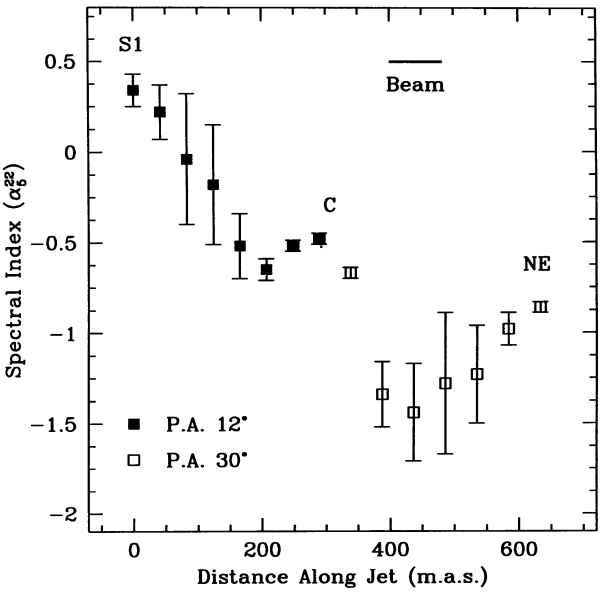

FIG. 5.—The 5–22 GHz spectral index of the jet emission as a function of distance along the jet (in milliarcseconds) from component S. Filled squares are taken from points along P.A. 12° (joining components S1 and C), and open squares are taken along P.A. 30° (joining components C and NE). Error bars are 3 σ.

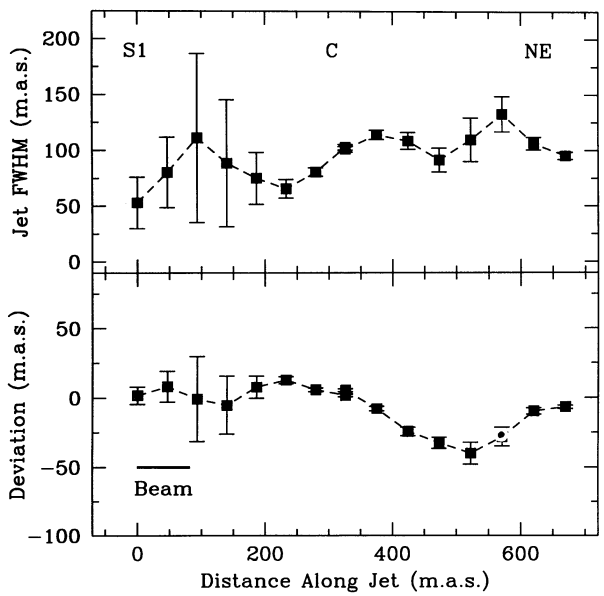

FIG. 6.—Properties of the extended jet emission as functions of distance along the jet. The measurements are from the 5 GHz MERLIN image. *Top panel:* The deconvolved cross-sectional width (FWHM) of the jet in milliarcseconds. *Bottom panel:* The deviation of the position of the peak surface brightness from a straight line joining adjacent components in milliarcseconds. Positive values mean displacements to the northwest. Error bars are 3 σ.

being introduced into the flow particularly at these sites, or alternatively that the flow is being compressed.

5.2. *The Jet Trajectory*

Based on the low surface brightness contours on the (1983) 1.3 cm VLA image, UNW describe the subarcsecond jet as being C-shaped indicating a gradual bending of the jet flow. In recalibrating the archival data, we found that the brightest jet emission follows a fairly straight path between the adjacent component. However, the exact shape of the contours outlining the low surface brightness emission varied with successive iterations of self-calibration. Furthermore, on the MERLIN 6 cm image, on which the steep-spectrum emission is much brighter, the jet also appears to follow straight lines joining the adjacent components.

To quantify the behavior of the jet, we traced the path of the jet on the (1992) 1.3 cm and MERLIN 6 cm images by first convolving both images up to the same resolution (0.″82, circular) and then extracting surface brightness cross sections of the jet along axes perpendicular to the lines joining the adjacent components. Consistent with the measurement errors, there are small differences in the displacement between the adjacent components on either image, so we took the cross sections from each image at equal spacings relative to the neighboring components. We measured the peak surface brightness, the projected jet width (FWHM), and the deviation of the jet from a straight line by fitting the cross-sectional surface brightness profiles with a single Gaussian.

The results are displayed in Figure 6. The jet broadens gradually on the path between components S1 and NE. The deconvolved widths are typically in the range 50–130 mas (5–13 parsecs) on the 5 GHz MERLIN image. The jet does not deviate strongly from a straight line path between adjacent components. Rather, measured on the 5 GHz MERLIN image the maximum displacement is ~40 mas (4 parsecs) to the southeast between components NE and C. This deviation is only 11% ± 1% of the projected distance separating components NE and C. The jet moreover does not curve into a C-shape; if this were the case the deviations would be consistently positive as they are plotted on Figure 6. Instead, the jet undergoes a sudden bend (from P.A. 11° in the south to P.A. 30° in the north) at component C but otherwise follows a fairly straight path between the adjacent components.

6. POLARIZATION

We have made naturally weighted images of the Q and U Stokes parameters for both the 1.3 cm B-array and 2 cm A-array data sets. The data were combined and corrected for the Ricean bias in the usual manner (e.g., Killeen, Bicknell, & Ekers 1986) to make images of the linear polarization. We have detected very weak polarization at 1.3 cm toward components NE and S. No significant polarization was detected toward the subarcsecond radio structure at 2 cm. At 1.3 cm, the linearly polarized flux at component NE (S) is 0.57 ± 0.12 mJy (0.51 ± 0.12 mJy), corresponding to a detection significance of 4.7 σ (4.3 σ). We therefore regard these detections as tentative. The beam-averaged fractional polarizations are 0.82% ± 0.18% and 0.80% ± 0.19% for components NE and S, respectively (the relative errors also take into account the noise on the total intensity image). These fractional polarizations are probably diluted by continuum emission from component C. The fractional polarization might be as large as ~3% taking into account this dilution. The alignment of the electric vectors are close to the orientation of the local jet axis (Fig. 7). We were unable to calibrate the polarization in the 1.3 cm A-array data due to a poor choice for the polarization standard, so we could not confirm this detection at higher

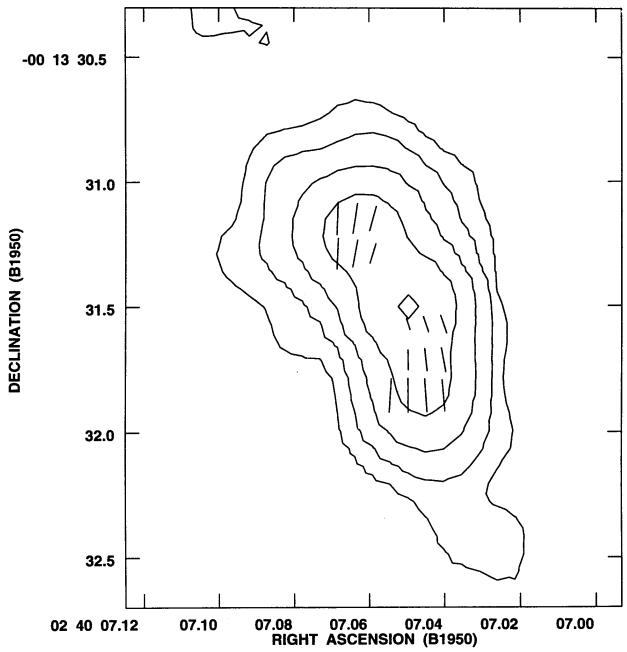

FIG. 7.—The linear polarization of the radio continuum emission at 22 GHz. The uniformly weighted 22 GHz continuum image is displayed in contours; the beam width is 0".26, roughly circular. The percent polarization vectors derived from naturally weighted images (beam width 0".4) are indicated by the straight, solid lines located at components NE and S.

resolution. At 2 cm wavelength, the 3 σ upper limits on the fractional polarization are less than 0.42% and less than 0.62% for components NE and S, respectively. Unlike the 1.3 cm values, these limits on the fractional polarizations are not diluted by confusion between the adjacent components.

Wilson & Ulvestad (1983) reported a 3 σ detection of linearly polarized emission toward the nucleus at 6 cm wavelength. The position angle of the electric vectors at 6 cm is $\sim 120°$, rotated from those observed at 1.3 cm. Taking these detections to be real, there is substantial depolarization between 1.3 and 2 cm wavelengths and perhaps repolarization between 2 cm and 6 cm. We explore the nature of the depolarizing medium in more detail in Paper II.

7. SUMMARY

In this paper we have presented new, subarcsecond resolution images of NGC 1068 that span the centimeter-wave radio regime. We have extracted the continuum spectra of and derived the spectral indices for the principal compact features (NE, C, S, S1, and S2). Cruder estimates of the spectra of the extended radio emission were also made. We have also analyzed the linear polarization and path of the radio jet. A summary of the principal results are listed as follows.

7.1. *Radio Continuum Spectra*

1. Component S overall has a very flat spectrum ($\alpha \sim -0.1$). Between 5 and 22 GHz the spectrum decomposes into contributions from subcomponent S1, which has an inverted spectrum ($\alpha \sim 0.3$); subcomponent S2, which is itself flat-spectrum ($\alpha \sim -0.15$); and a diffuse component whose spectrum is not well-determined by our observations ($\alpha = 0.38 \pm 0.44$). The brightness temperatures of the subcomponents are very low ($T_b \sim 3 \times 10^5$ K).

2. The radio spectrum of the jet joining the adjacent subarcsecond components steepens with distance from component S. A possible explanation is ageing of the synchrotron electrons along the jet axis, with the youngest material located near component S.

3. Component C also has a steep spectrum that is flatter (α[5–22 GHz] ~ -0.5) than the surrounding jet material. This result suggests that either the jet is compressed or that particles are reaccelerated at this site. In comparing the 5 and 22 GHz images, which have similar resolutions and spatial sensitivities, we find no evidence for a flat spectrum core at component C as suggested by UNW.

4. Component NE has a steep spectrum that is slightly flatter than that of the surrounding jet emission. The morphology of the radio emission surrounding component NE is irregular and does not everywhere align with the jet axis, suggesting an interaction with the surrounding ISM.

7.2. *Minimum Energy Properties*

The minimum pressures derived for the compact features are $P/k \sim 10^8$–10^9 K cm^{-3}, comparable to the global pressure inferred from line ratios for the NLR gas. The radio jet might be laterally confined by gas in the NLR.

7.3. *The Trajectory of the Radio Jet*

Contrary to the findings of UNW, we find no strong curvature in the path of the radio jet joining the principal subarcsecond components (NE, C, and S). Rather, the jet follows a fairly straight path between the adjacent components. At component C, therefore, the jet bends abruptly, rather than smoothly, by $\sim 20°$.

7.4. *Polarization*

We report the weak detection of low ($\lesssim 3\%$) linear polarization toward components S and NE on the 22 GHz images (0".25 resolution). No polarization is detected on the more sensitive 15 GHz images (0".13 resolution), confirming the results of UNW. If the polarization is real, then at 15 GHz the emission is depolarized by thermal plasma either foreground to the jet or entrained in the jet.

We wish to thank Maret Kukula and Tom Muxlow for contributing their data for this work. We also thank the referee, Jim Ulvestad, for providing suggestions that improved the clarity of the text and presentation. J. F. G. would like to recognize the extensive help and support provided by the faculty and staff at Jodrell Bank, particularly on the parts of Simon Garrington, Carole Mundell, and Tom Muxlow, and by the staff at NRAO Socorro. Meri Stanley (NRAO) was instrumental in helping us acquire and process the archival VLA data. J. F. G. also acknowledges support from the STScI Director's Discretionary Fund during part of the course of this work. Further support for this work was provided by NASA through grant number AR-04933.01-92A from the Space Telescope Science Institute, which is operated by the Association of Universities for Research in Astronomy, Inc., under NASA contract NAS5-26555. This paper represents a portion of J. F. G.'s Ph.D. thesis, to be submitted in partial fulfillment of the requirements of the Graduate School of the University of Maryland.

APPENDIX A

RESOLUTION OF THE COMPACT COMPONENTS

We describe here the filtering and measurement techniques and the results of the flux measurements. For convenience, we collectively refer to the MERLIN 18 and 21 cm data and the A-array 3.6 cm data as the "low-resolution" data, and we call the MERLIN 6 cm and the A-array 1.3 and 2 cm data the "high-resolution" data.

A.1. IMAGING TECHNIQUES

Due to the comparatively poor resolution of the "low-resolution" data, it was necessary to filter out the extended emission and "super resolve" the images to measure the flux densities of the compact components. The general imaging procedure used the conventional Fourier inversion technique followed by a CLEAN deconvolution, except that during the Fourier transform we included only those baselines longer than 200 kλ, corresponding to spatial scales $\lesssim 0\farcs5$. To minimize the confusion between adjacent continuum components, we also "superresolved" the images by convolving back the CLEAN components with a circular beam of width (FWHM) $0\farcs2$, intermediate between the widths of the major and minor axes of the formal Gaussian beams. The super-resolving beam overresolves by at most a factor of 1.5 along position angles lying generally northeast. A potentially problematic artifact resulting from the omission of short baselines is the "bowl effect," the symptom of which is a trough of negative signal surrounding the brighter continuum sources. Such artifacts appeared on the filtered images (see the inset to Fig. 1), but were typically at a low level. We were able to account for these artifacts partially by fitting a constant, negative offset with the elliptical Gaussians. The 18 cm image, so processed, is presented as an inset on Figure 1. The morphology of these high-pass filtered, superresolved images compare well with the "high-resolution" images, and, with the exception of the low-level "bowls," no obvious artifacts specifically resulted from the superresolution of the filtered images.

Although the spatial filtering and superresolution applied to the "low-resolution" images greatly reduces the confusion between the compact components and the extended emission, the (u, v) coverage of these filtered data still include baselines that are much shorter than those in the "high-resolution" data; that is, the filtered data may be more sensitive to emission extended on or near $\sim 0\farcs5$ scales. All of the compact component flux is, however, recovered by the relatively shorter baselines in the filtered data. Considering the remaining possibility of confusion with extended emission resulting from this short-spacing bias, the fluxes measured from the "low-resolution" images, are, in principle, upper limits to the true compact source fluxes. However, discussed in § 4.1, the spectral indices of the components measured from the "high-resolution" images generally compare well to those fitted to the fluxes measured from both the high- and low-resolution images, suggesting that the contribution of confused emission is small.

A.2. GAUSSIAN FITTING PROCEDURE

The components C and NE significantly brighten with increasing wavelength. As a result, even though the peaks of the three principal components are well-resolved by the $\lesssim 0\farcs2$ beams, the wings of the brightness distribution of components C and NE contribute significantly to the fluxes of their adjacent components measured in fixed apertures. For example, on the MERLIN 1.4 GHz image we estimate that as much as 25% of the flux density measured in an aperture surrounding component S is due to confusion with component C. To reduce the contribution of adjacent components to the measured fluxes, we performed an iterative Gaussian fit to each component on the low-resolution images as follows. First, we performed a two-Gaussian fit to the NE and C components and subtracted the resulting Gaussian model of component C from the image. Next, we measured the fluxes and dimensions of the NE and S components by fitting simultaneously a single Gaussian and a zero-level offset to each on the model-subtracted image. These models were in turn subtracted from the original image, and we repeated the single-Gaussian fitting for component C on the resulting model-subtracted image.

On the high-resolution images, this component-subtraction technique is unnecessary. Instead we just fit single Gaussians and zero-levels to the NE and C components. Furthermore, subcomponents S1 and S2 are at least partially resolved on these images, so the total flux density of component S is not properly measured by a single Gaussian fit; we instead fitted each subcomponent separately. We also measured the flux in a $0\farcs3$ square aperture enclosing both subcomponents for comparison with the single Gaussian fits to the "low-resolution" data. The position and characteristic size of component S were measured by the first and second intensity-weighted moments within the aperture. We also estimated the flux contained in the subcomponents by measuring higher order moments of the intensity and by single-Gaussian fits.

A.3. ESTIMATING THE PARAMETER UNCERTAINTIES

Since the formal errors computed from the covariance matrix are not in general good estimators of the Gaussian parameter uncertainties (they do not take into account, for example, the correlation between adjacent pixels), we used instead theoretical estimates for the uncertainties in the component parameters. Following Ball (1975) and Fomalont (1989), the uncertainty in the Gaussian peak, P, is estimated by the image rms, ΔP. We used instead the rms of the Gaussian model residual, so that the quality of the fit is also included in the error estimates; in this manner some account is given to the uncertainty resulting from confusion with extended emission. The uncertainty in position for a marginally resolved Gaussian is given by $\Delta X \simeq (\Delta P/P)\,(W/2)$, where W is the (beam-convolved) width of the Gaussian. The uncertainty in the width is given by $\Delta W \simeq (\Delta P/P)\,W$. We measured the beam-deconvolved widths of the principal components by a quadrature subtraction of the beam. The uncertainties in the beam-deconvolved widths were determined by varying the measured widths by $\pm 1\ \sigma$ and computing the corresponding deconvolved widths. Where the sources were unresolved in the lower error limit, we assigned a deconvolved source size of zero for recording purposes. Similarly, when a component was unresolved at a given frequency, we computed an upper limit by deconvolving the

upper 3 σ width of the measured source diameter. The uncertainty in the position angle of the elliptical Gaussian was estimated according to

$$\Delta(\text{p.a.}) \simeq 57.^{\circ}3\sqrt{\left(\frac{\Delta W_{\text{maj}}}{W_{\text{maj}}}\right)^2 + \left(\frac{\Delta W_{\text{min}}}{W_{\text{min}}}\right)^2},$$

where the maj and min subscripts refer to the major and minor axes, respectively. Finally, the uncertainty in the flux integrated over the Gaussian is obtained by an appropriate quadrature propagation of the uncertainties ΔP, ΔW_{maj}, and ΔW_{min}.

An important caveat regarding these uncertainty estimates is that they only crudely account for errors resulting from confusion. These estimates also ignore uncertainties resulting from systematic errors. According to the VLA Calibrator Manual, the relative uncertainty in the flux calibrations are small, on the order of 5%, compared to the measured statistical errors. Furthermore, as discussed above in § 4.1, the continuum fluxes measured on the low-resolution images compare favorably to that predicted from extrapolation of the high-resolution fluxes. Therefore, at each component the contribution of confusing flux to the low-resolution measurements is probably small compared to the measured total.

REFERENCES

Antonucci, R. 1993, ARA&A, 31, 473
Antonucci, R. R. J., & Miller, J. S. 1985, ApJ, 297, 476
Baars, J. W. M., Genzel, R., Pauliny-Toth, I. I. K., & Witzel, A. 1977, A&A, 61, 99
Ball, J. 1975, Methods Comput. Phys., 14, 177
Brinks, E., Skillman, E. D., Terlevich, R. J., & Terlevich, E. 1992, BAAS, 24, 1275
Burbidge, G. R. 1956, ApJ, 124, 416
Clark, B. G. 1980, A&A, 89, 377
Claussen, M. J., & Lo, K.-Y. 1986, ApJ, 308, 592
Fomalont, E. B. 1989, in Synthesis Imaging in Radio Astronomy, ed. R. A. Perley, F. R. Schwab, & A. Bridle (San Francisco: ASP), 219
Gallimore, J. F., Baum, S. A., & O'Dea, C. P. 1995a, ApJ, submitted (Paper II)
Gallimore, J. F., Baum, S. A., O'Dea, C. P., Brinks, E., & Pedlar, A. 1994, ApJ, 422, L13
———. 1995b, in preparation
Helfer, T. T., & Blitz, L. 1995, ApJ, in press
Högbom, J. 1974, ApJS, 15, 417
Jeffreys, W. H., Fitzpatrick, M. J., McArthur, B. E., & McCartney, J. E. 1988, GaussFit: A System for Least Squares and Robust Estimation (Austin: Univ. Texas)
Khachikian, E., & Weedman, D. 1971, Astrofizika, 7, 389
Killeen, N. E. B., Bicknell, G. V., Ekers, R. D. 1986, ApJ, 302, 306
Krolik, J. H., & Begelman, M. C. 1986, ApJ, 308, 55
———. 1988, ApJ, 329, 702
Krolik, J. H., & Lepp, S. 198, ApJ, 347, 179
Kukula, M. J., Pedlar, A., Baum, S. A., & O'Dea, C. P. 1995, MNRAS, in press
Macchetto, F., Capetti, A., Sparks, W. B., Axon, D. J., & Boksenberg, A. 1994, ApJ, 435, L15
Miller, J. S., Goodrich, R. W., & Mathews, W. G. 1991, ApJ, 378, 47
Moffet, A. T. 1975, in Galaxies and the Universe, Stars and Stellar Systems, Vol. 9, ed. A., Sandage, M., Sandage, & J. Kristian (Chicago: Univ. Chicago Press), 21
Muxlow, T. W. B. 1992, in Sub-arcsecond Radio Astronomy, ed. R. J. Davis & R. S. Booth (Cambridge: Cambridge Univ. Press), 252
Muxlow, T. W. B., Pedlar, A., Holloway, A., Gallimore, J. F., & Antonucci, R. R. J. 1995, MNRAS, submitted
Myers, S. T., & Scoville, N. Z. 1987, ApJ, 312, L39
Myers, S. T., & Spangler, S. R. 1985, ApJ, 291, 53
Neufeld, D. A., Maloney, P. R., & Conger, S. 1994, ApJ, 436, L127
Neff, S. G., et al. 1994, ApJ, 430, 545
Osterbrock, D., & Parker, R. 1965, ApJ, 141, 892
Pedlar, A., Booler, R. V., Spencer, R. E., & Stewart, O. J. 1983, MNRAS, 202, 647
Planesas, P., Scoville, N. Z., & Myers, S. T. 1991, ApJ, 369, 364
Scheuer, P. A. G., & Williams, P. J. S. 1968, ARA&A, 6, 321
Shields, G. A., & Oke, J. B. 1975, ApJ, 197, 5
Telesco, C. M., & Decher, R. 1988, ApJ, 334, 573
Ulvestad, J. S., Neff, S. G., & Wilson, A. S. 1987, AJ, 93, 22 (UNW)
van der Hulst, J. M., Hummel, E., & Dickey, J. M. 1982, ApJ, 261, L59
Watson, W. D., & Wallin, B. K. 1994, ApJ, 432, L35
———. 1987, ApJ, 319, 105
———. 1983, ApJ, 275, 8
Wilson, A. S., & Ulvestad, J. S. 1982, ApJ, 263, 576
Wynn-Williams, C. G., Becklin, E. E., & Scoville, N. Z. 1985, ApJ, 297, 607